JOURNAL OF THEORETICAL AND APPLIED MECHANICS
51, 3, pp. 649-660, Warsaw 2013

NUMERICAL INVESTIGATION OF THE INNER FLOW IN A CENTRIFUGAL PUMP AT THE SHUT-OFF CONDITION

Houlin Liu, Xianfang Wu, Minggao Tan

Research Center of Fluid Machinery Engineering and Technology, Jiangsu University, Zhenjiang, Jiangsu, China
e-mail: tmgwxf@gmail.com

The unsteady flow fields in a centrifugal pump at the shut-off condition (SOC) are simulated by the Unsteady Reynolds Averaged Navier-Stokes (URANS) approach. To improve simulation accuracy and assign the boundary condition, special 3D models are made. Three--dimensional URANS equations are solved on high-quality unstructured grids with the shear stress transport turbulence model by using the computational fluid dynamics (CFD) code CFX-11.0. Furthermore, the numerical simulation results are validated by particle image velocimetry (PIV) measurements. The main goal of the study is, on one hand, the validation of the numerical procedure proposed, and on the other hand, the detailed analysis of the unsteady inner flow field distribution and pressure fluctuation in the centrifugal pump at SOC. In addition, the head of the pump at SOC is predicted based on CFD results. The flow analysis indicates that there exists two eddies in each impeller flow passage, and the velocity at the volute diffusion part is very low. The amplitudes of pressure fluctuation at f_r (impeller rotation frequency) and $3f_r$ dominate in the impeller, while the pressure fluctuation at f_b (blade passing frequency) is dominant in the volute.

Key words: centrifugal pump, numerical simulation, shut-off condition, PIV

Nomenclature

b_2, b_3	–	width of blade outlet and volute inlet, respectively
D_1, D_2, D_3	–	diameter of impeller inlet, impeller outlet and volute inlet, respectively
F_t	–	area of volte throat
f_r, f_b	–	frequency of impeller rotation and blade passing, respectively
H, H_{so}	–	head at nominal condition and at SOC, respectively
n, n_s	–	rotation speed and specific speed $(3.65n\sqrt[4]{Q^2/H^3})$, respectively
Q, q	–	rate of flow and rate of leakage flow, respectively
Z	–	blade number
β_2	–	angle of blade outlet
η	–	efficiency at nominal condition

1. Introduction

Traditionally, hydraulic design for centrifugal pumps only considers the best efficiency point (BEP) requirements. Up to now, the traditional method is not feasible for modern centrifugal pumps such as pumps used in nuclear power plants and solar photovoltaic pumps. The former design needs considering more than 3 operation conditions, including characteristics at SOC (Yuan *et al.*, 2010), and the latter design should decrease pump power at SOC as much as possible to start the pump as soon as possible during a day (Short and Oldach, 2003). Therefore, to control the characteristics at SOC, it is currently urgent to study the inner flow field in centrifugal pumps at SOC.

With the development of computer technology and numerical methods, CFD has become a main tool to research the inner flow in fluid machinery. In the past, it was common practice to start the pump simulation with a steady assumption. The information provided by this approach is sufficient if only the mean flow is of interest. In general, a quite good agreement with experiments can be obtained from classical RANS computations. However, these models suffer from predicting details like flow separation or vortex. The flow inside a centrifugal pump at SOC is fully turbulent and highly unsteady, which requires an unsteady simulation. URANS and large eddy simulation (LES) are the two choices. Pure LES requires very fine and many grids, especially in boundary layers, and the generation of boundary conditions is more complex. Also, LES needs more computer resources (Lucius and Brenner, 2010). For these reasons, a turbulence resolving URANS model is used in the present investigation.

Because the boundary condition cannot be determined properly, the inner flow simulation at SOC for centrifugal pumps is still a problem. A literature review shows that related research is very few except Dyson *et al.* (2004), Dyson and Teixeira (2009) and Muggli *et al.* (2002). Muggli *et al.* investigated the flow field in a mixed flow pump with CFD and test, and pointed out that the flow field in the pump at a small flow rate ($Q < 0.25Q_{BEP}$) cannot be predicted by CFD because of the convergence problem. With some approximation and assumption, Dyson studied the inner flow in a centrifugal pump at SOC by using CFD, which consisted of an impeller having 3 curved blades with a double volute. Also, he predicted the pump head based on CFD results. Although his job is valuable, there is still something to be discussed. First, the shroud and hub cavity are not included in the computational zone, which has direct effects on the inner flow distribution and performance of the pump (Dong *et al.*, 2010). Second, some influence fators, such as calculation period and roughness (José *et al.*, 2006; José and Santolaria, 2006), are not considered in the simulation. Third, he did not do an inner flow experiment to validate CFD simulation, and the pressure fluctuation was not analyzed in detail. The last is that his research model is not normal, so the results may not be representative.

According to the above analyses, it can be known that there are still a lot of work to do to reveal the inner flow field distribution in centrifugal pumps at SOC. The objective of this study is twofold. First, based on Dyson's job, a better numerical modeling of the flow field in a centrifugal pump at SOC is carried out and validated. Second, flow patterns in the impeller and volute at SOC are obtained and analyzed carefully, so valuable conclusions about the flow structure at SOC are reported along the paper.

2. Numerical method

The URANS method is an efficient numerical method to capture transient phenomena in centrifugal pumps (José *et al.*, 2006; José and Santolaria, 2006). So in the present study, the URANS method is used to simulate the inner flow in a centrifugal pump at SOC, and the 3D URANS equations are solved using the CFX code.

2.1. Model description and grid

The pump has six backward column blades with a spiral volute. The detailed pump dimensions and performance data are shown in Table 1. The full flow field is considered to improve the simulation accuracy. The full three dimensional (3D) model is generated by Pro/E, and Fig. 1 shows the 3D model. A quarter of the 3D model is removed in Fig. 1 to display the interior structure of the pump. Given PIV test requirements, a semi-spiral suction is designed for the pump. From Fig. 1, it can be seen that the computational zone includes semi-spiral suction, impeller, volute, wear ring clearance, shroud chamber, hub chamber, and the impeller-volute

gap. Additionally, in order to set boundary conditions, the pump inlet and pump outlet are extended properly. The extension sections are too long to be presented in Fig. 1.

Table 1. Main parameters of the model pump

BEP					SOC	Geometry parameters							
Q [m^3h^{-1}]	H [m]	n [$r\,min^{-1}$]	n_s [–]	η [%]	H_{so} [m]	D_1 [mm]	z [–]	D_2 [mm]	b_2 [mm]	β_2 [°]	D_3 [mm]	b_3 [mm]	F_t [mm^2]
25.2	12.0	1450	68.6	58.4	12.79	75	6	198	9	39	220	33	1291

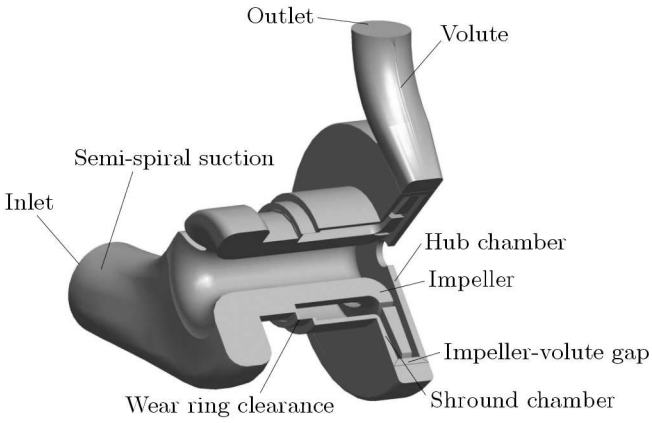

Fig. 1. Computational zone of the model

Because the pump structure is very complex, unstructured grid cells are generated to define the computational zones. The ICEM, preprocessor of CFX, is used to develop meshes. In order to check the influence of the grid on the results, meshes with different cell numbers are tested, and the test results are shown in Table 2. It indicates that the second and the third scheme have the same H_{so} prediction accuracy. But the third scheme needs more computation resource and time because of more cells.

Table 2. H_{so} prediction results for different grids

No.	Cell number	H_{so} simulation results [m]	H_{so} experiment results [m]	Prediction accuracy [m]
1	2638196	12.49	12.79	−0.50
2	3842435	12.77	12.79	−0.02
3	4976843	12.81	12.79	+0.02

Finally, the model has 3842435 cells in total, and the quality is satisfied. The quality of more than eighty percent of cells is larger than 0.8, and the quality of the worst cell is bigger than 0.3. The wall y^+ is controlled to stay at less than 20 in all the zones. The information between the static and rotation parts of the pump is transferred by using a sliding mesh technique.

During the mesh generation, special treatments are executed for the volute tongue and wear ring clearance because of their special structures. The volute tongue is distorted highly, and the radial dimension of the wear ring clearance is much smaller than its axial dimension. Therefore, the virtual block mesh and local refinement are used. The detailed grid and structure of the two parts are shown in Fig. 2.

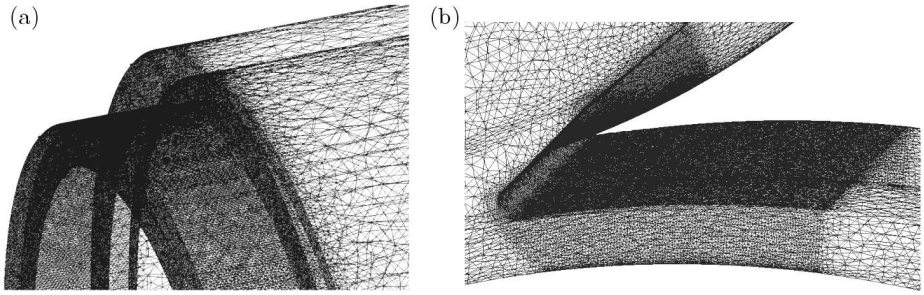

Fig. 2. Grid refinement of local parts; (a) wear ring clearance, (b) volute tongue

2.2. Boundary condition

As mentioned above, the inlet and outlet boundary conditions are very hard to determine according to the physical situation. At SOC, a lot of backflows occur in the pump inlet, and the pump outlet runs at the zero flowrate. In order to assign the inlet boundary condition, a feasible method is to build a proper 3D model. The inlet is extended twenty times the inlet pipe diameter to accept the backflow, and the outlet is extended four times the outlet pipe diameter to reflect the unsteady flow.

To set the outlet boundary condition, an assumption must be made. When a pump runs at SOC, the pump can be said to operate with a finite flow equal to the leakage flow through the wear ring. According to the analysis, the velocity outlet can be applied to the outlet boundary condition approximately, and the magnitude of leakage flow can be calculated from a formula by Guan (2011). In other words, an extremely small flow rate is used to approximate the zero flow rate

$$q = \frac{Q}{1 + 0.68\frac{1}{\sqrt[3]{n_s^2}}}$$

At solid walls, the no-slip condition with a logarithmic law for boundary layers is employed, and the roughness height is also considered according to the real condition.

2.3. Mathematical model

Considering incompressibility, viscosity and unsteadiness, the 3D URANS equations, which include the source term for the centrifugal force in the impeller, are solved by using the commercial code CFX. The effects of turbulence are modeled by using turbulence models. The calculation results obtained by different turbulence models are compared. The SST k-ω model is used to take the turbulence effects into account, because its simulation results are closest to the experimental results. The time-dependent term is a first-order implicit scheme. The second--order upwind scheme with numerical under-relaxation is applied for the discretization of the convection term, whereas the central difference scheme is applied for the discretization of the diffusion terms.

2.4. Numerical solution control

The simulations are parallelized in a high performance cluster with 16 nodes. The numerical calculations start with a steady simulation. The unsteady calculations are initialized from the steady simulation results. In order to reveal the transient flow in the pump at SOC, the determination of the time step and iteration cycles play a pivotal role, and many schemes are carried out. The two parameters can only be determined by comparison. The time step for the unsteady calculations is set to be $1.149 \cdot 10^{-4}$ s, which means that the impeller rotates 1 degree in a time

step. Finally, thirteen impeller revolutions are needed to achieve convergence for the periodic solutions. The number of iterations is adjusted to reduce the residual for a given variable in all cells below 10^{-4}. As the simulation is transient, it is necessary to store the data for every time step, which results in an output file of about 122 Gbytes.

3. CFD results and discussions

All the CFD results discussed in this part are from the thirteenth impeller revolutions. The pump head, inner flow field and pressure fluctuation at SOC will be discussed respectively and carefully.

3.1. Head at SOC

Figure 3 shows the pump head fluctuation at SOC in the impeller rotation period. It can be seen that there are six wave peaks and troughs, and the value of each peak and trough varies. The explanation for the former appearance is that the number of blades is six. The possible reason for the latter phenomena is that there is lots of unsteady flows in the pump at SOC. Therefore, the inner flow is very complex and transient. The average head of the curve is 12.77 m and the test head, as shown in Table 1, is 12.79 m. The deviation of the prediction head is very small, so the above CFD method is feasible.

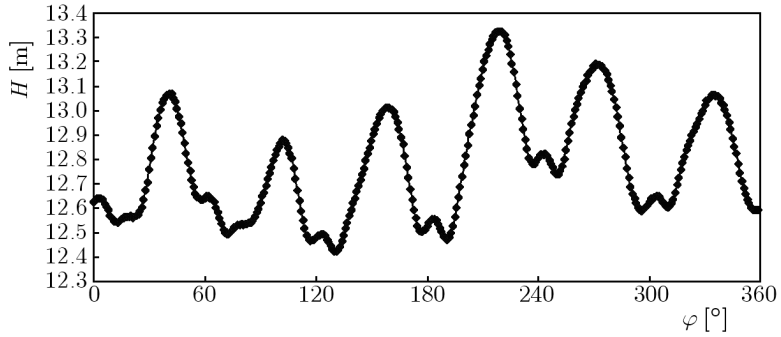

Fig. 3. Head fluctuation

3.2. Relative velocity distribution in the impeller

Figure 4 presents the relative velocity distribution in the impeller at different times. It illustrates that there are two eddies in each flow passage at any time, and one is very big, the other is small. The big one is at the blade suction side, and it almost blocks the whole flow passage. The small one is at the blade pressure suction side and near the impeller outlet. The velocity in the big eddy is all very low, while the velocity in the small eddy is all high. It can be called the rotation stall. Also, the jet-wake phenomenon is very evident in each flow passage at any time.

When the blade passes the volute tongue, the blade orientation effects caused by the impeller rotation are the most obvious. So, in the blade passing rotation $(2\pi/z\,\mathrm{rad})$, the inner flow in flow passage 1 is cared in detail. Figure 4a gives flow passage 1 orientation to the volute tongue, which is indicated by θ. When θ increases, the zone of the big eddy declines, while the zone of the small eddy becomes larger. With the increase of θ, the jet-wake phenomenon gets more obvious, and the maximum of relative velocity gets low.

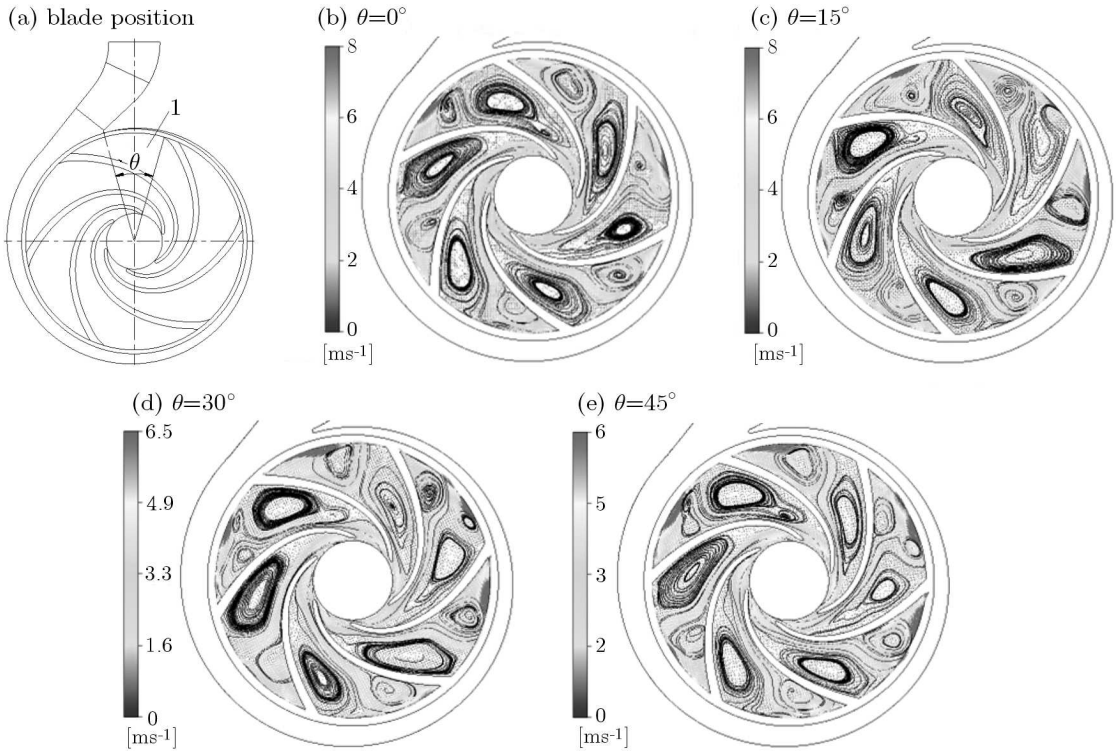

Fig. 4. Relative velocity distribution in the impeller at differene times [m/s]

3.3. Absolute velocity distribution in the pump

The absolute velocity distribution in the pump at different times are shown in Fig. 5. The impeller position in Fig. 5 is the same as that in Fig. 4. From Fig. 5, it can be seen that the absolute velocity distribution at SOC is different from that at the nominal condition obviously, especially for the velocity in the diffusion section of the volute. The velocity in the diffusion of the volute is very low, which means that the water here nearly does not flow and the flow circulation mainly occurs in the impeller and the spiral section of the volute. This is because that the rotation stall eddies block the impeller flow passages. Also, there is a big eddy in this diffusion zone, and it can result in eddy loss. From the stream line distribution, it can be concluded that a flow shock occurs at the volute tongue. As θ increases, the flow shock gets more obvious, which leads to more hydraulic loss. Except for flow passage 1 (as shown in Fig. 4), the absolute velocity distribution in the impeller and spiral section of the volute change little as the impeller rotates. With the increase of θ, the high velocity zone in flow passage 1 becomes larger.

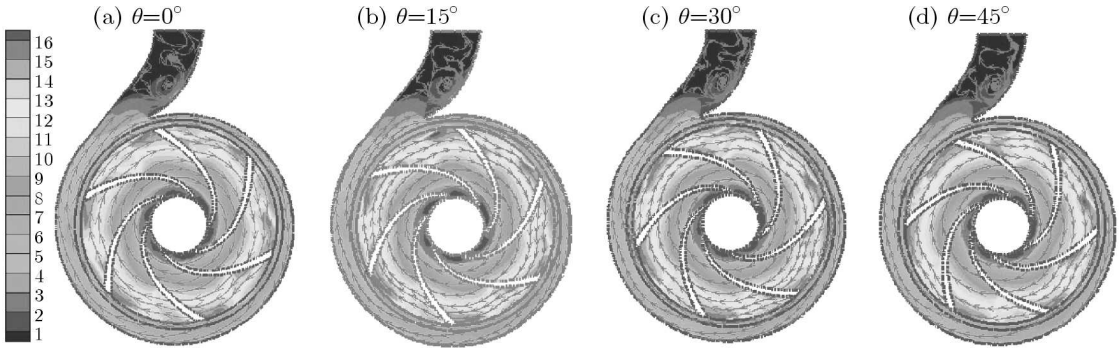

Fig. 5. Absolute velocity distribution in the pump [m/s]

3.4. Pressure fluctuation in the pump

In order to discover the pressure fluctuation rule in the pump, many monitoring points are set in the impeller and volute, as shown in Fig. 6. In total, there are 3 points in the impeller and 6 points in the volute. The position of these 9 points is uniform and representative. According to pressure at these 9 points, the pressure fluctuation from the impeller inlet to the volute outlet can be obtained and analyzed.

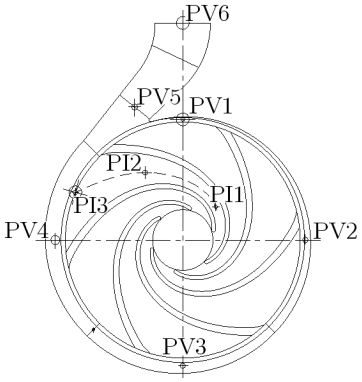

Fig. 6. Monitoring points in the pump

The pressure fluctuation in the impeller is indicated in Fig. 7. In time domain curves, there are 360 data on each curve. In order to distinguish each curve and present it clearly, only a part of the data in form of point symbols are shown on each curve. The frequency spectrum curves are obtained from time domain curves by fast Fourier transform (FFT). From Fig. 7a, it can be seen that the pressure fluctuation amplitudes at PI1 and PI2 are low, and the maximum fluctuation amplitudes at PI1 and PI2 are 3619 Pa and 8739 Pa, respectively. The pressure fluctuation at PI3 is very obvious, and the maximum fluctuation amplitude is 16085 Pa. The pressure fluctuation curves at PI1 and PI2 are flat, and there are apparent peaks on the pressure fluctuation curve at PI3. The above analyses indicate that the interactions between the impeller and volute have more and more effects as the impeller radius increases.

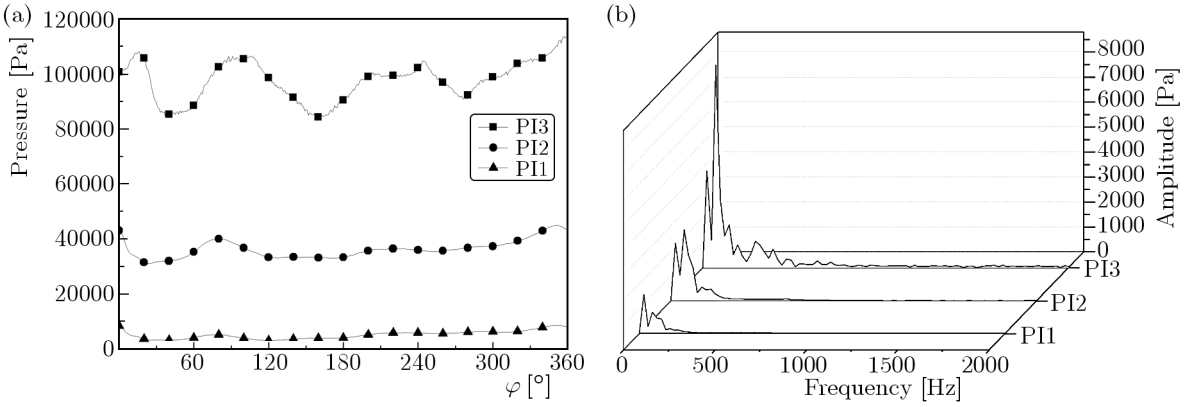

Fig. 7. Pressure fluctuation in the impeller, (a) time domain curves, (b) frequency spectrum curves

From Fig. 7b, it can be seen that the amplitudes of pressure fluctuation with frequencies for PI1, PI2, and PI3 are obviously different. For PI1, the maximum amplitude of pressure fluctuation is at 24.17 Hz, which is equal to fr (rotation frequency). For PI2 and PI3, the maximum amplitudes of pressure fluctuation are all at 72.5 Hz (3 fr). The second largest amplitude of pressure fluctuation for PI1, PI2 and PI3 is at 72.5 Hz, 24.17 Hz and 24.17 Hz, respectively. So, in the impeller, the amplitudes of pressure fluctuation at f_r and $3f_r$ dominate under SOC. There are

two possible reasons for such results. The first is that the rotation stall in the impeller is serious and the flow is unsteady. The second is that the gap between D_2 and D_3 is big, so pressure fluctuation at the blade passing frequency ($f_b = zf_r$) does not dominate.

The pressure fluctuation in the volute is shown in Fig. 8. From Fig. 8a, it can be seen that the pressure increases gradually from PV1 to PV6. The pressure fluctuation amplitude at PV1 is maximum, and the pressure fluctuation amplitude at PV4 is minimum, which means that the flow near the volute tongue is very unsteady. Beside the fluctuation amplitude curve at PV4, there are six peaks on each pressure fluctuation curve, which indicates that the rotator-stator interactions have more effects on the inner flow field in the volute. The pressure fluctuation at PV6 is very similar to that at PV5, because the velocity of flow in the volute diffusion part is very low, as analyzed in Fig. 5.

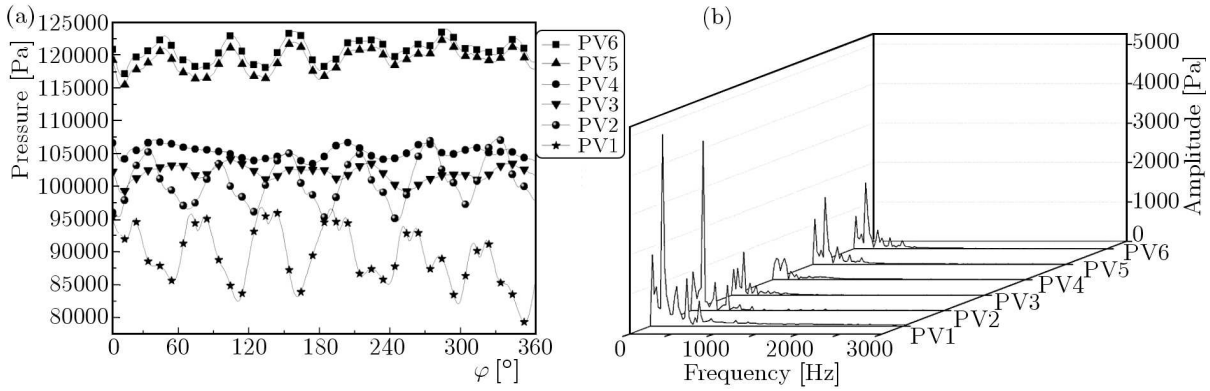

Fig. 8. Pressure fluctuation in the volute, (a) time domain curves, (b) frequency spectrum curves

From Fig. 8b, it can be seen that the amplitudes of pressure fluctuation with frequencies are obviously different from those in the impeller. The maximum amplitude of pressure fluctuation for all points in the volute is at 145 Hz, which indicates that the amplitudes of pressure fluctuation at f_b dominate in the volute. The second largest amplitudes of pressure fluctuation for all points are all low, and below 2000 Pa. The amplitude of pressure fluctuation for PV3 is the lowest among these points, because it is far away from the volute tongue. In conclusion, at SOC, the amplitudes of pressure fluctuation with frequencies in the volute are lower than those in the impeller.

4. PIV experiments

PIV has been successfully applied by several authors to obtain velocity fields in pumps (Westra *et al.*, 2010; Benra *et al.*, 2006). In order to validate the simulation results, the inner flow field in the pump at SOC has been tested at Jiangsu university by PIV.

4.1. Experiment description

To test the inner flow field by PIV, the test impeller and volute are made of transparent perspex. Corresponding to the unsteady simulation, four blade orientations are considered in the test, as shown in Fig. 4. The blades arrive at the next position after the impeller rotates by 15 degrees. So the impeller rotates 45 degrees in 4 different positions, which can reflect the inner flow field distribution in a rotation period as the impeller has six blades. All the measurements are conducted at the midspan. The encoder installed on the pump shaft is utilized to synchronize the measurement with the impeller position.

A PIV system from TSI has been utilized for the measurements. It consists of a YAG200--NWL pulse laser, whose single pulse energy is 200 mJ and frequency is 30 Hz. A digital camera

with a resolution of $2k \times 2k$ pixels is used for image acquisition. Al_2O_3 particles are employed as seeding particles, whose diameter is approximately $8\,\mu$m. The pump structure and optical solutions are presented in Fig. 9. A sketch of the test rig is shown in Fig. 10. In the experiment, the whole flow field can be obtained by PIV. But in fact, only the flow field in flow passage 4, 5 and 6 can be used to validate the simulation results, because the laser light in these 3 flow passages are the best. Overall, the error from PIV measurements is estimated to be 2%-3% (Liu *et al.*, 2012).

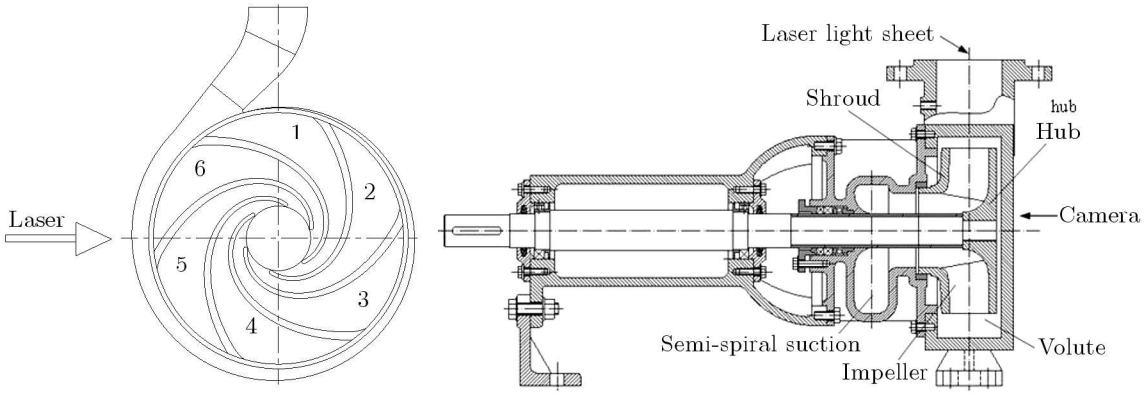

Fig. 9. Sketch of the test rig and light configuration

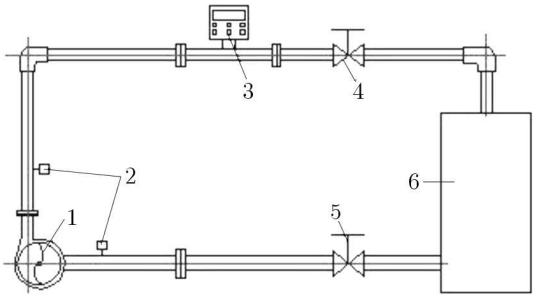

Fig. 10. Sketch of the test rig, 1 – pump, 2 – pressure transducer, 3 – electromagnetic flowmeter, 4 – outlet valve, 5 – inlet valve, 6 – water tank

4.2. Experiment results

As is known to us, from PIV test data, only the absolute velocity distribution can be obtained. So, in order to obtain the relative velocity, a velocity decomposition program has been developed according to the velocity triangle in centrifugal pumps. Figure 11 indicates the relative velocity distribution in the impeller obtained from a PIV test. It can be found that, as we analyzed above, the test data of the flow field in flow passage 1, 2 and 3 at each time are not good due to the weak laser light. So the test data of the rest flow field are compared with Fig. 4. By comparison, it can be found that the simulation results are not exactly the same as the test results. The small eddy near the impeller outlet is captured, the location, size and magnitude of the small eddy in simulation are greatly similar to those in the test. But the large eddy at the blade suction side does not occur in the test. The reasonable explanation for the comparison results is that the velocity of the large eddy is very low and lower than the dropping velocity of an Al_2O_3 particle. Therefore, the large eddy is not captured in the test.

In order to compare the experimental data and simulation results in detail, the absolute velocity data at point PI2 (as seen in Fig. 6) at different times are extracted from PIV test results and simulation results respectively. The absolute velocity data are presented in Fig. 12.

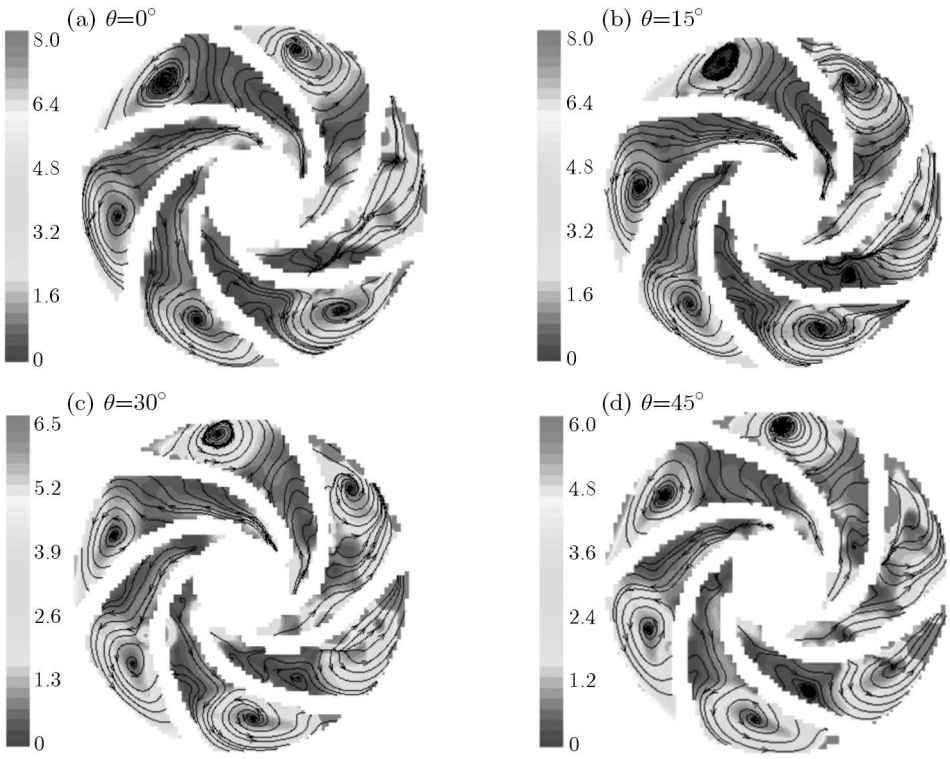

Fig. 11. Relative velocity distribution obtained from PIV

From Fig. 12, it can be concluded that the simulation results agree well with the PIV data. Also, the difference in the absolute velocity at point PI2 between the test and simulation data is very small. The biggest error of simulation is 2.44 percent $(\theta = 15°)$, the smallest error of simulation is 0.76 percent $(\theta = 45°)$. And the average error of simulation is 1.425 percent.

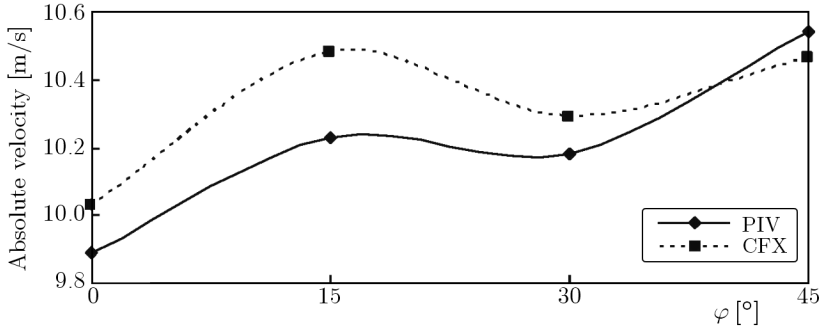

Fig. 12. Comparison of absolute velocity between PIV data and CFX data at point PI2

So, analyzing the results depicted in Figs. 11 and 12 one may conclude that the inner flow simulation for the centrifugal pump at SOC presented in this paper is successful.

5. Conclusions

In this paper, the inner flow field in a centrifugal pump at SOC is simulated and tested. The URANS is used for simulations and the PIV is used to carry out the test. Through the analyses on simulation and test results, the following conclusions can be obtained.

(1) To simulate the inner flow at SOC in a centrifugal pump with the URANS method, some special treatments should be given. The pump inlet and outlet must be extended properly

in the 3D model. During grid generation, local refinement and virtual block technologies are applied to deal with the volute tongue and wear ring clearance. A number of factors can only be determined by careful comparison in the numerical simulation, such as the turbulence model, time step, iteration cycles, and so on.

(2) The pump head curve at SOC in a cycle exhibits periodic fluctuation, but the fluctuation amplitudes of each peak are not the same, which is caused by the unsteady inner flow.

(3) There are two eddies in each impeller flow passage, one is small and the other is big. The velocity in the small eddy is high, and the velocity in the big eddy is very low. The big eddy nearly blocks the whole flow passage, which leads to poor flow rate circulation in the volute. So, the velocity in the volute diffusion part is very small. There is obvious a flow shock at the volute tongue as the impeller rotates.

(4) According to time domain pressure fluctuation curves, the rotator-stator interactions have more effects on the inner flow in the volute than that in the impeller. The amplitudes of pressure fluctuation at f_r and $3f_r$ dominate in the impeller, while the pressure fluctuation at f_b is dominant in the volute.

(5) In order to capture the inner flow with low velocity in the pump by PIV, a kind of seeding particles with better tracking performance is needed.

Acknowledgments

The authors gratefully acknowledge the financial support of National Natural Science Foundation of China under Project No. 51109095, 51079062, National Natural Science Foundation of Jiangsu Province under Project No. BK2010346, graduate student scientific innovation foundation of Jiangsu Province No. CXLX11_0576, and a Project funded by the Priority Academic Program Development of Jiangsu Higher Education Institutions.

References

1. Benra F.-K., Dohmen H.J., Sommer M., 2006, Flow field visualization of a single-blade centrifugal pump using PIV-method – comparison to numerical results, *Journal of Visualization*, **9**, 4, 358-358
2. Dong L., Liu H.-L., Tan M.-G., et al., 2010, Study on key issues of the whole flow field numerical simulation for centrifugal pump, *Proceedings of the 2010 International Conference on Pumps and Fans*, October 18-21, Hangzhou China
3. Dyson G., Teixeira J., 2009, Investigation of closed valve operation computaional fluid dynamics, *Proceedings of the ASME 2009 Fluids Engineering Division Meeting*, August 2-6, Vail, Colorado, USA
4. Dyson G., Teixeira J., Ivey P.C., 2004, Closed valve flow field investigation using computational fluid dynamics, *2004 ImechE Event Publications*, **130**, 1-16
5. Guan X., 2011, *Theory and Design for Modern Pumps*, Yuhang Press, Beijing [in Chinese]
6. José G., Parrondo J., Santolaria C., et al., 2006, Steady and unsteady radial forces for a centrifugal pump with impeller to tongue gap variation, *Journal of Fluids Engineering*, **128**, 454-462
7. José G., Santolaria C., 2006, Unsteady flow structure and global variables in a centrifugal pump, *Journal of Fluids Engineering*, **128**, 937-946
8. Liu H.L., Wang K., Yuan S.Q., et al., 2012, 3D PIV test of inner flow in a double blade pump impeller, *Chinese Journal of Mechanical Engineering*, **25**, 3, 491-497
9. Lucius A., Brenner G., 2010, Unsteady CFD simulation of a pump in part load conditions using scale-adaptive simulation, *International Journal of Heat and Fluid Flow*, **31**, 1113-1118

10. Muggli F.A., Holbein P., Dupont P., 2002, CFD Calculation of a mixed flow pump characteristic from shutoff to maximum flow, *Journal of Fluids Engineering*, **124**, 798-802

11. Short T.D., Oldach R., 2003, Solar powered water pumps: the past, the present – and the future, *Journal of Fluids Engineering*, **125**, 1, 76-82

12. Westra R.W., Broersma L., van Andel K., et al., 2010, PIV measurements and CFD computations of secondary flow in a centrifugal pump impeller, *Journal of Fluids Engineering*, **132**, 6, 061104-8

13. Yuan S., Fu Q., Zhu R., 2010, Multi-operating- condition hydraulic design of centrifugal charging pump for nuclear power plant, *Journal of Drainage and Irrigation Machinery Engineering*, **28**, 3, 185-189 [in Chinese with English abstract]

Manuscript received June 20, 2012; accepted for print November 19, 2012